Check for updates

# Radiation of the high-order plasmonic modes of large gold nanospheres excited by surface plasmon polaritons†

Jing-Dong Chen, ‡[a] Jin Xiang, ‡[a] Shuai Jiang,[a] Qiao-Feng Dai,[a] Shao-Long Tie[b] and Sheng Lan ✱[a]

Large metallic nanoparticles with sizes comparable to the wavelength of light are expected to support high-order plasmon modes exhibiting resonances in the visible to near infrared spectral range. However, the radiation behavior of high-order plasmon modes, including scattering spectra and radiation patterns, remains unexplored. Here, we report on the first observation and characterization of the high-order plasmon modes excited in large gold nanospheres by using the surface plasmon polaritons generated on the surface of a thin gold film. The polarization-dependent scattering spectra were measured by inserting a polarization analyzer in the collection channel and the physical origins of the scattering peaks observed in the scattering spectra were clearly identified. More interestingly, the radiation of electric quadrupoles and octupoles was resolved in both frequency and spatial domains. In addition, the angular dependences of the radiation intensity for all plasmon modes were extracted by fitting the polarization-dependent scattering spectra with multiple Lorentz line shapes. A significant enhancement of the electric field was found in the gap plasmon modes and it was employed to generate hot-electron intraband luminescence. Our findings pave the way for exploiting the high-order plasmon modes of large metallic nanoparticles in the manipulation of light radiation and light–matter interaction.

## 1 Introduction

Nanoparticles of noble metals, especially gold (Au) nanoparticles, have attracted great interest in the last two decades owing to their superior physical properties and chemical stability and have found potential applications in the areas of nanophotonics,[1–8] biophotonics,[3,9] and biomedicine.[10,11] The existence of a strongly localized electric field on the surfaces of Au nanoparticles, such as gold nanospheres (GNSs) and gold nanorods (GNRs) can be utilized to significantly enhance the linear[12–20] and nonlinear[21–27] optical responses of the neighboring nanomaterials.

Since the sizes of conventional GNSs are much smaller than the diffraction limit of visible light, they are generally resolved by using a dark-field microscope which detects the

light scattered by GNSs. Based on Mie theory,[28] the scattering of a small GNS with a diameter smaller than 100 nm is dominated by its electric dipole (ED) resonance which appears at ~530 nm. Thus, such a small GNS will behave as a dipole, which exhibits a doughnut-shaped radiation pattern,[14,19,29–32] under the excitation of linearly polarized light. The corresponding extinction is dominated by absorption rather than scattering which is generally quite weak.

Due to the difficulty in the synthesis and fabrication of GNSs with large diameters ($d$) by using either chemical or physical methods,[15,16,19,33] previous studies on the scattering of GNSs are limited mainly to small GNSs that exhibit only ED radiation. However, it has been shown that the high-order electrical resonances in plasmonic nanostructures (*e.g.*, nanorings) may exhibit excellent directional scattering due to the coherent interaction between ED and electric quadrupole (EQ) and this feature has been exploited in the design of nanoantennas with highly directional radiation.[34] Based on Mie theory,[35] the ED resonance of a GNS will be shifted into the near infrared spectral range and high-order resonances, such as EQ and electric octupole (EOC), will emerge in the visible light spectrum on increasing the diameter of the GNS. Owing to the large overlap between the ED and EQ (or the EQ and EOC) resonances, the coherent interaction between the ED and EQ in a GNS with $d$

*[a]Guangdong Provincial Key Laboratory of Nanophotonic Functional Materials and Devices, School of Information and Optoelectronic Science and Engineering, South China Normal University, Guangzhou 510006, China. E-mail: slan@scnu.edu.cn*
*[b]School of Chemistry and Environment, South China Normal University, Guangzhou 510006, China*
†Electronic supplementary information (ESI) available. See DOI: 10.1039/C8NR02099J
‡These authors contributed equally to this work.

~340 nm or that between the EQ and EOC in a GNS with $d$ ~560 nm will lead to highly directional radiation (see Fig. S1 in the ESI†). At the wavelength where the generalized Kerker condition[34] is satisfied (*i.e.*, the amplitudes of the two high-order resonances are equal), the constructive interference in the forward direction leads to a significantly enhanced scattering intensity while the destructive interference in the backward direction results in considerably suppressed scattering intensity. From this point of view, a large GNS supporting high-order electric resonance acts as a simple and efficient plasmonic nanoantenna when it operates at the wavelength where the generalized Kerker condition is fulfilled.[34] Therefore, the investigation of the radiation of high-order plasmon modes, such as EQ and EOC, has become increasingly important not only for fundamental research[21] but also for practical application.[36,37]

Apart from the surface plasmon resonances (SPRs) excited in single metallic nanoparticles (*e.g.*, GNSs or GNRs), the interaction between a metallic nanoparticle and a thin metal film has received a significant amount of attention because such an all-metallic plasmonic system can be employed to realize nanoscale photonic devices with different functions.[14–18,23,24,38–42] The existence of the thin metal film will modify the SPR of the metallic nanoparticle through the introduction of the mirror image for the ED,[14,43,44] which is manifested in the scattering spectrum of the metallic nanoparticle. In addition, gap plasmon modes with a significantly enhanced electric field,[41] which can be exploited to enhance Raman scattering[45] and photoluminescence,[24,39] may be introduced in the narrow gap between the metallic nanoparticle and the metal film. Such all-metallic plasmonic systems exhibit several advantages over other coupled plasmon resonators that support gap plasmon modes, including their ease of fabrication, their highly reproducible optical response, their structural stability, and their wideband spectral tunability through the variation of the particle-film separation.[24] In addition, such gap plasmon modes can also be resolved in the scattering spectrum of the metallic nanoparticle.[15] More importantly, the existence of the thin metal film makes it possible to excite the metallic nanoparticle with the surface plasmon polaritons (SPPs) generated on the surface of the thin metal film, leading to a significantly enhanced scattering light.

So far, the excitation of GNSs with the SPPs generated on a thin Au film is limited for GNSs with dimensions smaller than 80 nm.[14] In this case, the interaction between the ED of the GNS and its mirror image is weak.[14,39,46] The major reason is the difficulty in the synthesis of GNSs with large diameters. Although the synthesis of GNSs with diameters as large as ~200 nm was reported by using a chemical method,[33] the morphology of GNSs did not appear to be spherical. Recently, the observation of the gap plasmon modes between a GNS and a gold film was reported for GNSs with diameters as large as ~150 nm fabricated by using an epitaxial method.[15] Unfortunately, the scattering of a GNS with $d$ ~150 nm is still dominated by ED resonance.

In this article, we reported on the fabrication of high-quality GNSs with diameters ranging from 80 to 560 nm on a thin Au film by using femtosecond (fs) laser ablation. The scattering spectra of such GNSs excited by the SPPs generated on the surface of the Au film were measured by using an inverted dark-field microscope. We analyzed the various plasmon modes induced in the GNSs and their contributions to the total scattering light of the GNSs. The scattering spectra of the GNSs were characterized by using a polarization analyzer and the radiation patterns were recorded by using a coupled charge device (CCD). The two-dimensional (2D) radiation patterns of various plasmon modes (*i.e.*, angular dependence of the scattering light) were successfully extracted by de-convolution of the polarization-dependent scattering spectra measured using a polarization analyzer. We also revealed the radiation patterns originating from the coherent interaction of several plasmon modes and the significantly enhanced electric field in the gap plasmon modes of large GNSs which can be employed to generate efficient hot-electron intraband luminescence.[47,48]

## 2 Experimental and numerical methods

### 2.1 Sample preparation

We employed fs laser ablation to fabricate GNSs with diameters ranging from 80–560 nm. In experiments, 800 nm fs laser light delivered by using a fs amplifier (Legend Elite, Coherent) with a pulse duration of 90 fs and a repetition rate of 1 kHz was focused on the surface of a 50 nm thick Au film by using a lens with 22 mm focal length. The ejected GNSs with different diameters were randomly distributed on the Au film along the two sides of the ablated line. The morphologies and sizes of the as-prepared GNSs were examined by scanning electron microscopy (SEM) (Ultra55, Zeiss) observations.

### 2.2 Optical characterization

The scattering properties of GNSs excited either by using white light in a conventional dark-field microscope or by using the SPPs generated on the surface of the Au film were characterized by using an inverted microscope (Axio Observer A1, Zeiss) equipped with a spectrometer (SR-500i-B1, Andor) and a full-color CCD (DS-Ri2, Nikon). In conventional dark-field microscopy, white light was incident on the Au film at an angle of ~33° with respect to the normal of the surface. In comparison, a slightly focused *p*-polarized white light with a diameter of ~2 mm was shined on the Au film at an incidence angle of ~45.8° to excite the SPPs with a broadband (see Fig. S2 in the ESI†). The scattering light of GNSs was collected with a 100× objective (NA = 0.7–1.3, Plan-NEOFWAR, Zeiss) in the forward direction and analyzed by inserting a polarization analyzer in the collecting channel. A fs laser (Mira 900S, Coherent) with a pulse duration of ~130 fs and a repetition rate of 76 MHz was employed to excite the hot electron luminescence of GNSs.

### 2.3 Numerical modeling

The scattering spectra of GNSs were either analytically calculated based on Mie theory or numerically simulated by using the finite-difference time-domain (FDTD) technique. The permittivity of Au was fitted from the experimental data.[49] For the simulation of the scattering spectra of GNSs excited by white light in conventional dark-field microscopy, we used a total-field/scattered-field source to simulate the scattering efficiencies of GNSs excited by plane waves incident normally on the Au film from the silica substrate. Differently, a slightly focused Gaussian beam with an incidence angle of 45.8° was employed to simulate the scattering spectra of GNSs excited by the SPPs. The scattering fields of GNSs excited by the SPPs were calculated by using a standard two-step method by which the total scattering field and background field in the absence of GNSs were calculated separately. Two monitors symmetrically placed at a distance of 1000 nm apart from the Au film surface were used to record the electric and magnetic field distributions. The areas of the monitors were chosen to be 16 000 × 16 000 nm$^2$ when calculating the scattering efficiency and to be 26 000 × 26 000 nm$^2$ when calculating the far-field radiation patterns. Based on the calculated scattering fields and the Poynting vectors, and their components as well, the scattering efficiencies and far-field radiation patterns of GNSs excited by the SPPs without or with polarization analyzed could be obtained. In order to obtain converged simulation results, the mesh size used in the gap region was 0.15 nm while that used in the GNS and Au film was 1.00 nm. A perfectly matched layer boundary condition was employed to terminate the finite simulation region.
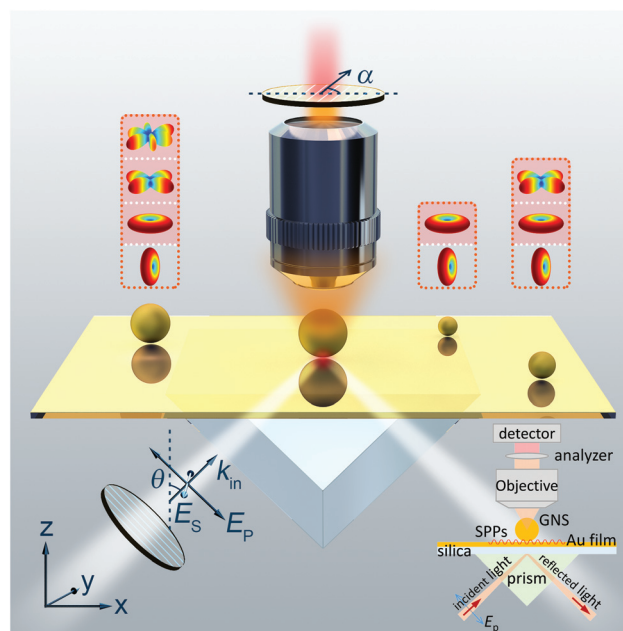


**Fig. 1** Schematic showing the excitation of a GNS with the SPPs generated on the surface of a thin Au film and the detection of the scattering light by using an objective lens. The SPPs were generated in the Otto configuration where a slightly focused white light with *p* polarization ($E_p$) was shined on the Au film at an angle of $\theta \sim$45.8°. A polarization analyzer whose polarization angle is defined with respect to the *x* direction (angle $\alpha$ in the figure) was inserted in the collection channel to eliminate the *x* or *y* component of the scattering light. The plasmon modes excited in GNSs with different diameters, including ED, EQ and EOC, are represented by the typical radiation patterns of these plasmon modes. A simplified schematic showing the experimental setup is given in the inset.

## 3 Results and discussion

Fig. 1 shows the schematic of exciting a GNS with the SPPs generated on the surface of a thin Au film and detecting the scattering light of the GNS in the forward direction by using the objective lens of a microscope connected to a spectrometer. Au nanoparticles with spherical shape and smooth surface (*i.e.*, GNSs) were fabricated by fs laser ablation of a 50 nm thick Au film deposited on a silica substrate (see Fig. S3 in the ESI†). The as-prepared GNSs with different diameters were randomly distributed on the thin Au film (see Fig. S4 in the ESI†). These GNSs could be excited by either the evanescent wave or the SPPs generated on the surface of the Au film, depending on the angle of the incident light. Since the SPPs can only be generated by using *p*-polarized light, we consider only the plasmon modes induced by the horizontal and vertical components of the electric field of the *p*-polarized light (*i.e.*, $E_x$ and $E_z$). Based on Mie theory, the plasmon modes of GNSs induced in the visible to near infrared range depend on their diameters. The lowest-order plasmon mode EDs ($p_x$ and $p_z$) will exist in all GNSs even though their diameters are as small as 20 nm. The second-order plasmon mode EQ ($e_q$) will emerge for GNSs with diameters larger than 220 nm while the high-order plasmon mode EOC ($e_{oc}$) will appear in GNSs with

diameters larger than 380 nm (see Fig. S5 in the ESI†). When the high-order plasmon modes, such as $e_q$ and $e_{oc}$, are shifted into the visible to near infrared spectral range, the low-order ones (*i.e.*, EDs) will be moved to much longer wavelengths which are beyond the detection wavelength range of our detector (400–1000 nm). In addition to the plasmon modes induced in GNSs, two gap plasmon modes ($g_x$ and $g_z$) may be created between the GNS and the Au film for GNSs with *d* > 80 nm. While the resonant wavelength of $g_x$ depends mainly on the diameter of the GNS, the resonant wavelength of $g_z$ is determined mainly by the gap width (*g*) between the GNS and the Au film. In order to resolve the high-order plasmon modes, a polarization analyzer was inserted in the collection channel which could be employed to eliminate the radiation from horizontally-oriented EDs ($p_x$ and $g_x$) and to identify vertically-oriented EDs ($p_z$ and $g_z$) which are insensitive to the polarization angle of the analyzer. More importantly, the use of the polarization analyzer makes it possible to extract the angular-dependent scattering (*i.e.*, 2D radiation pattern) of various plasmon modes, providing further evidence for identifying the nature of plasmon modes. Moreover, owing to the existence of the Au film, the mirror images of various plasmon modes ($p_{xm}$, $p_{zm}$, $e_{qm}$, $e_{ocm}$) also need to be taken into account

because the scattering of GNSs in the far field is determined by the coherent interaction of the plasmon modes and their mirror images.

### 3.1 Scattering of GNSs excited by the evanescent wave

The scattering of the GNSs placed on the thin Au film can be characterized by using conventional dark-field microscopy. In this case, the incidence angle $\theta$ of the illuminating white light on the back surface of the Au film is estimated to be ~33° and no SPPs are generated on the front surface of the Au film. Therefore, the GNSs are excited by the evanescent wave on the front surface of the Au film. Since the evanescent wave is very weak, especially in the long-wavelength region, the radiation of high-order plasmon modes, such as the EQ and EOC of a large GNS, will hardly be resolved in the scattering spectrum.

In Fig. 2, we present the scattering spectra of GNSs with different diameters on the thin Au film measured by using conventional dark-field microscopy. The SEM images of the



**Fig. 2** Forward scattering spectra (blue curves) of GNSs with different diameters placed on a thin Au film measured by using conventional dark-field microscopy. The illuminating white light was incident on the Au film at an angle of ~33° and the scattering light in the forward direction was detected. Scattering spectra calculated by using the FDTD method (red curves) are also provided for comparison. The gap width between the GNS and the Au film was assumed to be $g$ = 1.00 nm in the numerical simulations. SEM images of the GNSs and CCD images of the scattering light are shown in the insets. The length of the scale bar is 100 nm in all cases.

GNSs and the CCD images of the scattering light are shown in the insets. The scattering spectra simulated by using the FDTD method (red curves in Fig. 2) are also provided for comparison and they are in good agreement with the measured ones. In all cases, two scattering peaks can be identified in the scattering spectrum. On increasing the diameter of the GNS, the scattering peak at the short wavelength remains nearly unchanged (~530 nm). In contrast, the scattering peak at the long wavelength is red shifted and its intensity decreases rapidly. Since the incidence angle is small in dark-field microscopy measurements, the scattering of vertically-oriented EDs and multipoles is negligible because of the significantly attenuated electric field of the illuminating light after passing through the Au film, and only the horizontally-oriented EDs contribute to the forward scattering. For a small GNS, there exist two horizontally-oriented EDs. One is the ED induced in the GNS ($p_x$) and the other is the ED created at the gap between the GNS and the Au film ($g_x$). Owing to the existence of the Au film, however, the magnetic dipole (MD, $m_y$) induced at the contacting point between the GNS and the Au film due to the coherent interaction between $p_x$ and its mirror image $p_{xm}$ should be taken into account (see Fig. S6 in the ESI†). In most cases, the radiation of $g_x$ is invisible in the scattering spectrum because the scattering spectrum is dominated by the radiation of $m_y$. However, $g_x$ may appear as a small shoulder in rare cases (see Fig. S7 in the ESI†). Thus, the scattering peak at the long wavelength is attributed to $m_y$ arising from the coherent interaction between $p_x$ and $p_{xm}$. As the diameter of the GNS is increased, the distance between $p_x$ and $p_{xm}$ becomes larger, leading to the redshift of the scattering peak.[47] In addition, the reduced scattering intensity is caused by the larger reflection of the illuminating light at long wavelengths. The scattering peak at ~530 nm arises from the peak transmission of the Au film because the GNS is actually excited by the evanescent wave on the front surface of the Au film. If the scattering spectrum of the GNS is normalized by using the transmission spectrum of the Au film instead of the spectrum of the illuminating light, then the scattering peak will become a small shoulder or disappear (see Fig. S8 in the ESI†). This assignment is further verified by replacing the Au film with a silver (Ag) film whose transmission peak appears at ~330 nm. In that case, the scattering peak at the short wavelength appears at ~330 nm and it disappears when the scattering spectrum is normalized by using the transmission spectrum of the Ag film (see Fig. S9 in the ESI†).

As mentioned above, the radiation of high-order plasmon modes of a GNS is not resolved in the scattering spectrum of the GNS measured by using conventional dark-field microscopy. In most cases, they are smeared by the strong scattering peak at ~530 nm, as shown in Fig. 2. In order to resolve the high-order plasmon modes, we need to enhance the excitation efficiencies of the high-order plasmon modes on the one hand and suppress the scattering peak at ~530 nm on the other hand. From this viewpoint, the excitation of GNSs by using the SPPs generated on the surface of the Au film appears to be an effective way to characterize the radiation of the high-order plasmon modes of GNSs.
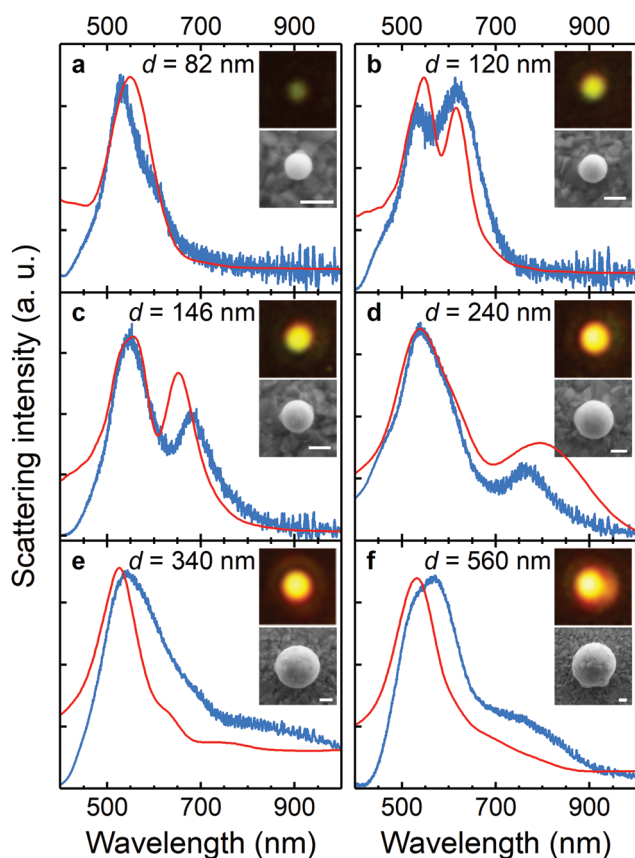
## 3.2 Scattering of GNSs excited by SPPs

The SPPs on the surface of the Au film, which were used to excite the GNSs, were generated by using $p$-polarized white light in an Otto configuration,[50] as depicted in Fig. 1. In this case, the incidence angle is larger than the critical angle for total internal reflection, which is estimated to be 43°. A significantly enhanced electric field is created on the surface of the Au film which is quite suitable for exciting the EQ and EOC of a large GNS (see Fig. S10 in the ESI†). For a large GNS, the scattering light involves mainly the contributions from the ED ($p_x$), EQ ($e_q$), EOC ($e_{oc}$) induced by the horizontal component of the electric field ($E_x$) and their mirror images (*i.e.*, $p_{xm}$, $e_{qm}$, and $e_{ocm}$). In addition, the vertically-oriented ED ($p_z$) induced by the vertical component of the electric field ($E_z$) is no longer negligible because of the significantly enhanced electric field in the $z$ direction. More importantly, the gap plasmon modes ($g_x$ and $g_z$) also contribute significantly to the scattering light owing to the dramatically enhanced electric field in the SPPs. Apparently, the simultaneous excitation of various plasmon modes makes the analysis of the scattering spectra more complicated. Fortunately, one can identify the physical origins of the scattering peaks by inspecting the evolution of the resonant wavelength on increasing the diameter of the GNS and the variation of the scattering intensity on increasing the polarization angle of the analyzer. For example, the resonant wavelength of $g_z$ is determined mainly by the gap width $g$ and

it is not sensitive to the change in the diameter. In addition, the scattering intensity of $g_z$ should be independent of the polarization angle of the analyzer. Based on these two features, we can easily identify the scattering peak resulting from $g_z$. In contrast, a redshift of the resonant wavelength is expected for $p_x$ and $g_x$ and their radiation can be completely removed by setting the polarization analyzer perpendicular to the $x$ direction ($\alpha$ = 90°). With the help of the polarization analyzer, the scattering properties of the EQ and EOC of a large GNS can be resolved in frequency (*i.e.*, scattering peaks) and spatial (*i.e.*, scattering patterns) domains after eliminating the radiation of horizontally-oriented EDs.

**Radiation of different plasmon modes revealed in spectra.** In Fig. 3, we present the scattering spectra of GNSs with different diameters which are excited by using the SPPs generated on the surface of the Au film. In each case, the scattering spectra were measured by rotating the polarization analyzer with an increment of 10° (see Fig. S11 in the ESI†) and the scattering patterns were recorded accordingly by using a CCD. For the GNS with $d$ = 82 nm (Fig. 3a), one can see a scattering peak with two shoulders in the scattering spectrum measured at $\alpha$ = 0°. They correspond to the contributions of $p_x$, $g_x$ and $p_z$ whose peaks are located at 540, 580 and 620 nm, respectively. The radiation of $p_x$ and $g_x$ can be completely removed by setting $\alpha$ = 90°. In this case, only a scattering peak located at 620 nm is observed, corresponding to $p_z$. This assignment is further confirmed by examining the evolution of the scattering
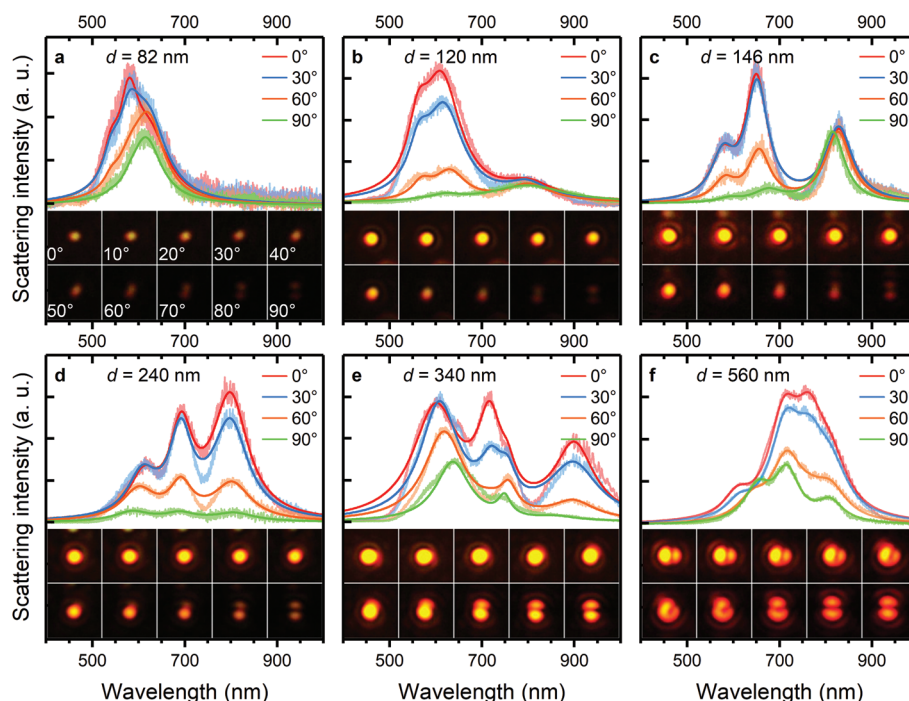


**Fig. 3** Scattering spectra measured for SPP-excited GNSs with different diameters of (a) $d$ = 82, (b) $d$ = 120, (c) $d$ = 146, (d) $d$ = 240, (e) $d$ = 340, and (f) $d$ = 560 nm by setting the polarization analyzer at different polarization angles ($\alpha$) of 0°, 30°, 60°, and 90°. The fittings of the polarization-dependent scattering spectra by using multiple Lorentz line shapes corresponding to different modes are also provided (solid lines with darker colors). The CCD images of the scattering light recorded by setting the polarization analyzer at different polarization angles ($\alpha$) with an increment of 10° are shown in the insets.

pattern shown in the inset. For $\alpha = 0°$, only a bright spot is observed because the scattering light is governed by the two horizontally-oriented EDs (*i.e.*, $p_x$ and $g_x$). When $p_x$ and $g_x$ have been completely eliminated, two spots aligned in the $y$ direction (*i.e.*, for $\alpha = 90°$) are observed in the scattering pattern, in good agreement with the radiation of a vertically-oriented ED (*i.e.*, $p_z$) filtered by using a polarization analyzer. For the GNS with $d = 120$ nm (Fig. 3b), the situation is quite similar to that observed in the GNS with $d = 82$ nm except for the appearance of $g_z$. Owing to the increase in the diameter, however, the resonant wavelengths of $p_x$, $g_x$ and $p_z$ are red shifted to 560, 620, and 800 nm, respectively. For $\alpha = 90°$, only the radiation of $p_z$ at 800 nm and that of $g_z$ at 620 nm are left in the scattering spectrum. Since $g_z$ is determined mainly by the gap width $g$ between the GNS and the Au film, it is not sensitive to the change in the size of the GNS. It is noticed that the largest red-shift of the resonant wavelength is observed in $p_z$, in good agreement with the previous observations.[15] In the scattering spectra of the GNS with $d = 146$ nm (Fig. 3c), the three scattering peaks, which are attributed to the radiation of $p_x$ (580 nm), $g_x$ and $g_z$ (650 and 670 nm), and $p_z$ (820 nm), are well separated because the redshifts of these modes are different. It is remarkable that the scattering intensity of $p_z$ is independent of the polarization angle, verifying the vertical orientation of $p_z$. In this case, the scattering peak of $g_z$ resolved at $\alpha = 90°$ appears at ~670 nm, which is slightly different from the previous cases (*i.e.*, $d = 120$ nm, Fig. 3b) due to the small difference in gap width.

When the diameter of the GNS is further increased to $d = 240$ nm (Fig. 3d), one can still observe three scattering peaks in the visible to near-infrared spectral range for $\alpha = 0°$. They are attributed to the radiation of $e_q$ (610 nm), $g_x$ and $g_z$ (690 nm), and $p_x$ (800 nm), respectively. For $\alpha = 90°$, three scattering peaks can be identified in the scattering spectrum. Here, it is noticed that the scattering spectrum obtained for $\alpha = 0°$ looks quite similar to that of the GNS with $d = 146$ nm (Fig. 3c, $\alpha = 0°$). For $\alpha = 90°$, the scattering peak at ~800 nm ($p_x$) almost disappears for the GNS with $d = 240$ nm while the scattering peak at ~820 nm ($p_z$) remains nearly unchanged for the GNS with $d = 146$ nm. This difference shows clearly the different radiation properties of $p_x$ and $p_z$ modes. Besides, the radiation of $p_x$ cannot be completely removed by using the cross-polarized analyzer, implying that the cross section of the GNS on the $xy$ plane is an ellipse rather than a circle, and the electric field in the $x$ direction excites a small amount of ED in the $y$ direction. It is also interesting to note that the radiation of $e_q$ begins to appear at ~610 nm. Its intensity decreases on increasing the polarization angle. However, its radiation does not disappear even at $\alpha = 90°$, which is in good agreement with the EQ nature. In addition, the scattering pattern observed at $\alpha = 90°$ is composed of two orange spots aligned in the $y$ direction, which originates from $e_q$. For GNSs with $d > 200$ nm, $p_z$ is shifted to wavelengths longer than 950 nm, which is not detected by our spectrometer.

For the larger GNS with $d = 340$ nm (Fig. 3e), the situation becomes more complicated. The scattering spectrum

measured at $\alpha = 0°$ is dominated by four scattering peaks which can be assigned to the radiation of $e_q$ (610 nm), $g_x$ (720 nm), $g_z$ (760 nm), and $p_x$ (900 nm), respectively. At $\alpha = 90°$, the radiation of $g_x$ at 720 nm and that of $p_x$ at 900 nm are completely eliminated. As a result, the radiation of $g_z$ peaking at 760 nm is clearly identified in the scattering spectrum. In this case, two gap plasmon modes $g_x$ and $g_z$ are separated in frequency domain and this phenomenon is observed only in large GNSs. The resonant wavelength of $e_q$ is red shifted to 630 nm for $\alpha = 90°$ and its intensity is attenuated to half of its original value. In this case, the scattering pattern is dominated by that of $e_q$ which exhibits two orange lobes aligned in the $y$ direction. Since the scattering pattern of $g_z$ is expected to exhibit two red spots aligned in the $y$ direction with smaller size and weaker intensity, it is smeared by the scattering pattern of $e_q$ which governs the scattering pattern at $\alpha = 90°$. Therefore, we observe for the first time the 2D radiation pattern of an EQ in a large GNS excited by SPPs, which is a big challenge from the experimental point of view. The achievement of high-quality GNSs with large diameters on a thin Au film by using fs laser ablation in combination with the use of SPP excitation and a cross-polarized analyzer makes it possible to clearly identify the radiation of an EQ in both the frequency and spatial domains.

The largest GNS obtained by fs laser ablation has a diameter of $d = 560$ nm, as shown in the inset of Fig. 2f. In the scattering spectrum measured at $\alpha = 0°$, one can find three scattering peaks at 630, 710, and 760 nm and a small shoulder at 810 nm. The three scattering peaks originate from the radiation of $e_{oc}$, $g_z$, and $g_x$, and the small shoulder arises from the radiation of $e_q$. At $\alpha = 90°$, one can clearly identify $e_{oc}$, $g_z$ and $e_q$ peaking at 660, 710, and 800 nm, respectively. The contribution of $g_x$ is completely filtered out. Although the radiation pattern of the GNS at $\alpha = 90°$ contains the contributions of $e_q$ and $e_{oc}$, it is apparent that the radiation pattern of $e_{oc}$ is dominant. It also appears as two lobes aligned in the $y$ direction but with a larger size. In addition, the scattering light appears as red. Although we cannot completely remove the radiation of $e_q$ and observe the radiation of pure $e_{oc}$, it is still a big progress in the observation of the radiation from the high-order plasmon modes in large GNSs. Since the resonant wavelengths of $e_q$ and $e_{oc}$ are much different, the radiation of a pure EOC can be observed by adding an appropriate high-pass filter in the collection channel.

For $e_q$ in the GNS with $d = 340$ nm and $e_{oc}$ in the GNS with $d = 560$ nm, it is noticed that there exists an obvious change in the resonant wavelength when the polarization angle $\alpha$ is changed (see Fig. S11 and S12 in the ESI†). This behavior can be easily understood if we examine the scattering spectra of the two GNSs which have been decomposed into the contributions of various plasmon modes (see Fig. S13 in the ESI†). For the GNS with $d = 340$ nm, there exists a large overlap between the EQ and ED. In addition, there exists a smaller overlap between the EQ and EOC which is not considered in the fitting of the scattering spectra. As a result, a red shift of the scattering peak of the $e_q$ is observed on increasing the

polarization angle. Similarly, a large overlap of the EOC and EQ is observed for the GNS with $d = 560$ nm. The small overlap between the EOC and electric hexadecapole (EHEX), which is not taken into account in the fitting of the scattering spectra, is thought to be responsible for the redshift of the scattering peak of $e_{oc}$.

Relying on the excitation of the SPPs and the polarization analyzer inserted in the collection channel, we were able to identify the resonant peaks of various plasmon modes induced in GNSs with different diameters in the scattering spectra of the GNSs. For clarity, the resonant peaks appearing in the scattering spectra obtained by setting $\alpha = 0°$ and $90°$ and their assignments are summarized in Table 1.

**Radiation of different plasmon modes revealed in space.** As shown in the above analysis, we can identify the physical origins of the scattering peaks observed in the scattering spectra of GNSs with different diameters excited by the SPPs with the help of a cross-polarized analyzer. Actually, the scattering spectra with multiple peaks can be decomposed into the contributions of various plasmon modes by fitting the polarization-dependent scattering spectra with multiple Lorentz line shapes (see Fig. S12 in the ESI†). The fitting results of the scattering spectra have been presented in Fig. 3 in solid curves which show excellent agreement with the measured spectra. By fitting the scattering spectra measured at different polarization angles, we have derived the angular dependence of the radiation intensity on the $xy$ plane for various plasmon modes that contribute to the total scattering, as shown in Fig. 4. In Fig. 4a, we show the angular dependence of the radiation intensity derived for $p_x$, $g_x$, and $p_z$ of the GNS with $d = 82$ nm. While $p_x$ and $g_x$ exhibit a typical radiation pattern of an ED oriented in the $x$ direction (i.e., an 8-like

**Table 1** Plasmon modes revealed in the polarization-dependent scattering spectra of GNSs excited by SPPs

| Diameter of GNS | Polarization angle $\alpha$ | ED ($p_x$) | $g_x$ | $g_z$ | ED ($p_z$) | EQ | EOC |
|---|---|---|---|---|---|---|---|
| 82 nm | 0 | 540 nm | 580 nm | / | 620 nm | / | / |
| | 90 | — | — | | 620 nm | | |
| 120 nm | 0 | 560 nm | 620 nm | 620 nm | 800 nm | / | / |
| | 90 | — | — | 620 nm | 800 nm | | |
| 146 nm | 0 | 580 nm | 650 nm | 670 nm | 820 nm | / | / |
| | 90 | — | — | 670 nm | 820 nm | | |
| 240 nm | 0 | 800 nm | 690 nm | 680 nm | >1000 nm | 610 nm | / |
| | 90 | — | — | 680 nm | | 580 nm | |
| 340 nm | 0 | 900 nm | 720 nm | 760 nm | >1000 nm | 610 nm | / |
| | 90 | — | — | 760 nm | | 630 nm | |
| 560 nm | 0 | >1000 nm | 760 nm | 720 nm | >1000 nm | 810 nm | 630 nm |
| | 90 | | — | 720 nm | | 800 nm | 660 nm |

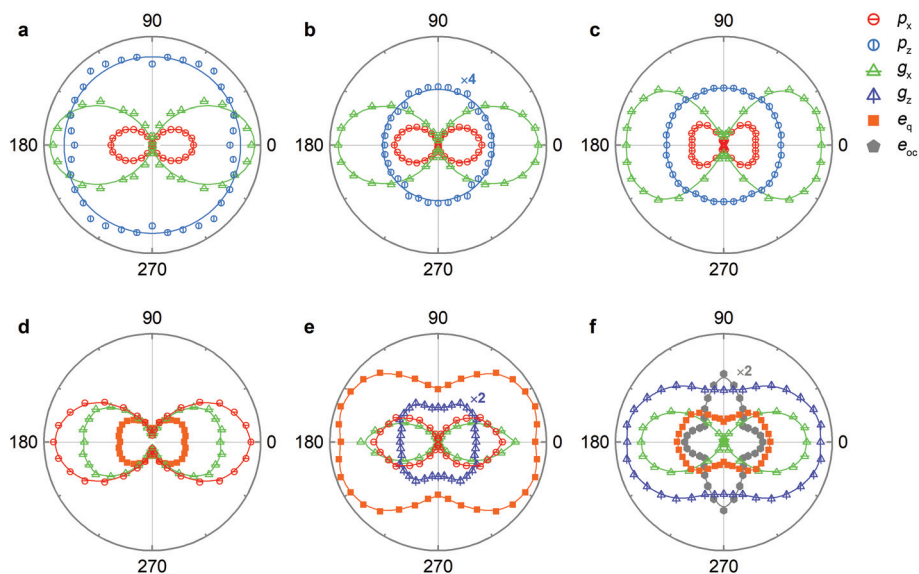"—" stands for the eliminated modes when setting $\alpha = 90°$; "/" stands for the negligible modes.



**Fig. 4** Angular dependence of the scattering light intensity on the $xy$ plane extracted for the ED ($p_z$ and $p_{zm}$, $p_x$ and $p_{xm}$, $g_z$, and $g_x$), EQ ($e_q$ and $e_{qm}$) and EOC ($e_{oc}$ and $e_{ocm}$) induced in SPP-excited GNSs with different diameters of (a) $d = 82$, (b) $d = 120$, (c) $d = 146$, (d) $d = 240$, (e) $d = 340$, and (f) $d = 560$ nm.

shape), $p_z$ shows the radiation pattern of a typical ED oriented in the $z$ direction (*i.e.*, a circle). It can be seen that the radiation intensity of $p_z$ is stronger than $p_x$ and $g_x$ because of the small diameter of the GNS. In this case, the GNS is effectively excited by the $z$ component of the electric field of the SPPs which are strongly localized on the Au film. In addition, a strong coherent interaction between $p_z$ and its mirror image $p_{zm}$ is expected because of the small distance between them, leading to a strong scattering intensity. For the GNS with $d$ = 120 nm (Fig. 4b), the situation is similar to that observed in the GNS with $d$ = 82 nm except for the reduction in the radiation intensity of $p_z$. For the GNS with $d$ = 146 nm (Fig. 4c), it is noticed that the radiation patterns of $p_x$ and $g_x$ deviate from the standard radiation pattern of a typical ED (*i.e.*, an 8-like shape). It is probably caused by the excitation of a small amount of ED oriented in the $y$ direction. In the GNS with $d$ = 240 nm (Fig. 4d), the angular dependence of the radiation intensity for $e_q$ has been deduced. The 2D radiation pattern of $e_q$ is revealed more clearly in the GNS with $d$ = 340 nm (Fig. 4e). On the $xy$ plane, the maximum radiation intensities of $e_q$ are achieved at 30°, 150°, 210°, and 330°. In the GNS with $d$ = 560 nm (Fig. 4f), we obtain the radiation pattern of $e_{oc}$ on the $xy$ plane. Different from the radiation pattern of $e_q$, the maximum radiation intensities of $e_{oc}$ are observed at 0°, 90°, 180°, and 270°.

**Simulated radiation patterns of different plasmon modes.** Although we can identify different plasmon modes that contribute to the forward scattering with the help of a cross-polarized analyzer, the scattering light at a certain wavelength generally involves the contributions of a few plasmon modes. In order to gain a deep insight into the scattering light of the GNSs, we have simulated the three-dimensional (3D) radiation patterns at the scattering peaks for GNSs with $d$ = 150 and 240 nm, as shown in Fig. 5. Since a broadband SPP was gener-

ated by using slightly focused white light in the experiments, a Gaussian beam instead of a plane wave was used in the numerical simulations. It is found that the simulated scattering spectra are in good agreement with the measured ones. Fig. 5a shows the scattering spectra measured and simulated for the GNS with $d$ = 150 nm in the absence of the polarization analyzer and by setting the polarization angle at 0° and 90°. In the scattering spectra measured and simulated without using the polarization analyzer, one can see three scattering peaks located at 573, 647, and 879 nm, which correspond to $p_x$, $g_x$ and $p_z$, respectively. The 3D radiation patterns calculated at 573, 647, and 879 nm are shown in Fig. 5b–d. The radiation patterns at 573 and 647 nm involve the contributions of two EDs oriented in the $x$ direction (*i.e.*, $p_x$ and $g_x$) and they appear to be similar. It is noticed that the radiation patterns at both wavelengths are much different from the radiation pattern of a typical ED oriented in the $x$ or $y$ direction because of the coherent interaction between $p_x$ and $g_x$. In addition, both radiation patterns are not symmetric with respect to the $z$ axis because the SPPs are generated by using oblique incident light. Differently, the radiation pattern at 879 nm, which originates mainly from an ED oriented in the $z$ direction ($p_z$), looks like the radiation pattern of a vertically-oriented ED although it is modified slightly by coupling. Even so, these three radiation patterns coincide well with the results of the previous report.[19] In Fig. 5e, we show the scattering spectra simulated and calculated for the GNS with $d$ = 240 nm. In this case, one can see three scattering peaks appearing at 610, 690, and 800 nm, which correspond to the radiation of $e_q$, $g_x$ and $p_x$. Since the resonant wavelengths of $e_q$ and $g_x$ are too close, the radiation patterns calculated at 610 and 690 nm are quite similar, as shown in Fig. 5f and g. They involve the contributions of both $e_q$ and $g_x$ which interact coherently. Consequently, the radiation pattern is different from that observed in the GNS with
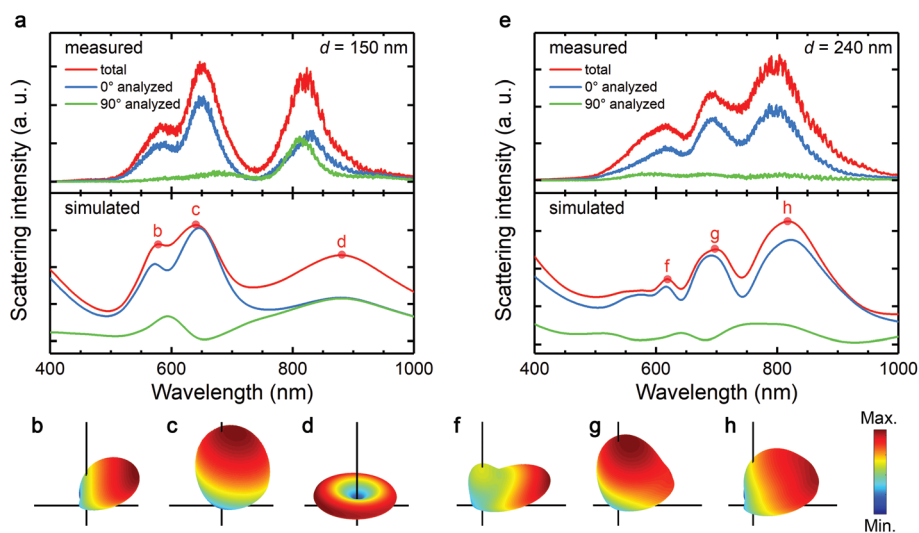


**Fig. 5** Scattering spectra measured and simulated for SPP-excited GNSs with $d$ = 150 nm (a) and 240 nm (e) with $g$ = 1.00 and 0.30 nm, respectively. The 3D radiation patterns calculated at the three scattering peaks for the GNSs with $d$ = 150 and 240 nm are shown in (b–d) and (f–h), respectively.
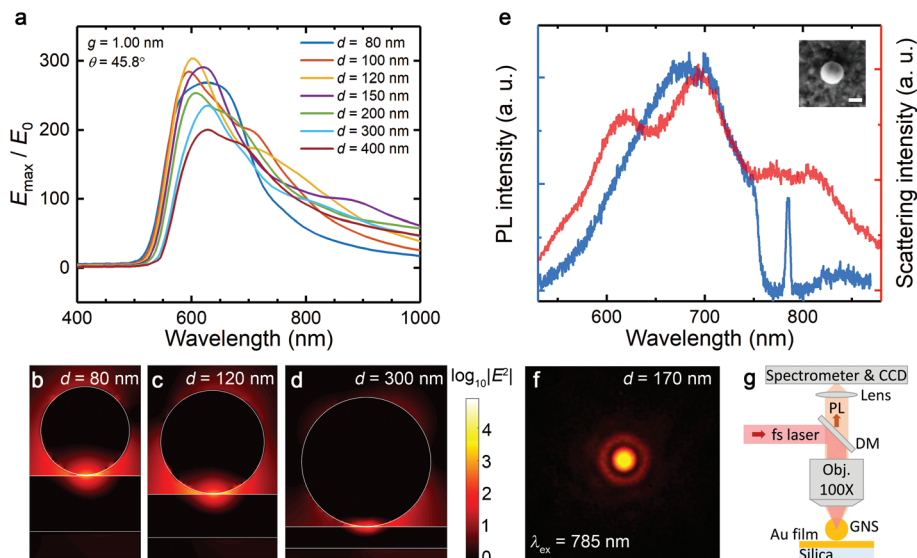
**Fig. 6** (a) Spectra of the maximum electric field enhancement factor ($E_{max}/E_0$) calculated for GNSs with different diameters with a fixed gap width of $g = 1.00$ nm. The maximum electric field enhancement is achieved at the contacting point between the GNS and the Au film. The electric field distributions on the $xz$ plane calculated for three typical GNSs with $d = 80$, 120, and 300 nm are shown in (b), (c), and (d), respectively. (e) Luminescence spectrum (blue) of a large GNS excited by using fs laser light with a laser power of 0.10 mW. The scattering spectrum (red) of the GNS is also provided for reference and the SEM image of the GNS is shown in the inset. (f) Emission pattern recorded by using a CCD. (g) Schematic of experimental setup for exciting and detecting the hot luminescence of GNSs. DM: dichroic mirror.

$d = 150$ nm which originates from the coherent interaction of two EDs ($p_x$ and $g_x$). Although the radiation pattern at 800 nm is dominated by $p_x$, it involves a small contribution of $g_x$. The coherent interaction between them results in a radiation pattern shown in Fig. 5h.

### 3.3 Electric field enhancement in gap plasmon modes and generation of hot luminescence

It has been known that a strongly localized electric field can be achieved for the gap plasmon modes (*i.e.*, $g_x$ and $g_z$) at the contacting point between the GNS and the Au film,[14,24,39] especially in the case when the gap width $g$ is very small (see Fig. S14 in the ESI†). Since the scattering spectrum is quite sensitive to the gap width, we can estimate the gap width by comparing the calculated spectrum with the measured one. For example, the gap width for the GNS with $d = 240$ nm was estimated to be $g = 0.30$ nm because the spectrum calculated by using $g = 0.30$ nm matches well with the measured one. For a fixed gap width of $g = 1.00$ nm, we can calculate the wavelength dependence of the maximum enhancement factor for the electric field on the $xz$ plane, which is achieved at the contacting point between the GNS and the Au film, for GNSs with different diameters ranging from 80 to 400 nm, as shown in Fig. 6a. In each case, it can be seen that the wavelength where the maximum enhancement factor is achieved is red shifted on increasing the diameter of the GNS. The largest enhancement factor, which is more than 300, is obtained in the GNS with $d = 120$ nm. Since the enhancement of electric field at the contacting point may be induced by either the gap plasmon modes ($g_x$ and $g_z$) or the magnetic dipole ($m_y$) resulting from

the coherent interaction of $p_x$ and $p_{xm}$, a broadband enhancement of electric field is observed over a wide wavelength range of 600–800 nm in all cases. The electric field distributions on the $xz$ plane calculated for GNSs with $d = 80$, 120, and 300 nm are shown in Fig. 6b–d. It is confirmed that the maximum electric field is achieved at the contacting point between the GNS and the Au film. Since the enhancement factors of electric field larger than 100 can still be obtained for wavelengths longer than 700 nm, the GNSs placed on the Au film can be effectively excited by using fs laser light. By doing so, we were able to observe efficient hot electron luminescence from the large GNSs, as shown in Fig. 6e and f. Different from the down-converted luminescence generated by exciting the gap plasmon mode of a small GNS with single-photon excitation,[39] the hot electron luminescence observed in the large GNS is composed of both the up- and the down-converted parts. It originates from the two-photon excitation of the gap plasmon mode and belongs to hot-electron intraband luminescence which is similar to blackbody radiation.[48] It means that the all-metallic system composed of a large GNS and a thin metal film can be employed to generate efficient hot-electron intraband luminescence under the excitation of fs laser light.

## 4 Conclusions

In summary, we have successfully fabricated high-quality GNSs with different diameters on a thin Au film and investigated systematically the scattering properties of such GNSs excited by the SPPs generated on the surface of the Au film. It is found that the scattering light involves the contributions of various

plasmon modes, including horizontally- and vertically-oriented EDs, EQ and even EOC. The coherent interaction between these plasmon modes and their mirror images leads to the scattering peaks in the scattering spectra. By inserting a polarization analyzer in the collection channel and varying the polarization angle, one can clearly identify the physical origins of various scattering peaks. The SPP excitation in combination with the use of a cross-polarized analyzer makes it possible to resolve the radiation of EQ and EOC in both the frequency and spatial domains. In addition, the angular dependence of the scattering intensity for different modes can be extracted by fitting the scattering spectra with multiple Lorentz line shapes. It is revealed that the radiation pattern at a certain wavelength is generally determined by the coherent interaction of two or more plasmon modes and deviates from the radiation pattern of pure ED or EQ. It is shown that the significantly enhanced electric field with an enhancement factor larger than 300 achieved in the gap plasmon mode can be employed to generate efficient hot-electron intraband luminescence. Our findings are quite helpful for designing plasmon nanoantennas based on the coherent interaction of ED and EQ (or EQ and EOC) and plasmon sensors and even lasers based on the gap plasmon modes.

## Conflicts of interest

There are no conflicts to declare.

## Acknowledgements

## References

1 P. Zijlstra and M. Orrit, *Rep. Prog. Phys.*, 2011, **74**, 106401.
2 P. Zijlstra, J. W. M. Chon and M. Gu, *Nature*, 2009, **459**, 410–413.
3 J. N. Anker, W. P. Hall, O. Lyandres, N. C. Shah, J. Zhao and R. P. Van Duyne, *Nat. Mater.*, 2008, **7**, 442–453.
4 F. Hao, Y. Sonnefraud, P. Van Dorpe, S. A. Maier, N. J. Halas and P. Nordlander, *Nano Lett.*, 2008, **8**, 3983–3988.
5 Z. Fang and X. Zhu, *Adv. Mater.*, 2013, **25**, 3840–3856.
6 J. Olson, A. Manjavacas, L. Liu, W.-S. Chang, B. Foerster, N. S. King, M. W. Knight, P. Nordlander, N. J. Halas and S. Link, *Proc. Natl. Acad. Sci. U. S. A.*, 2014, **111**, 14348–14353.
7 H. R. Ren, X. P. Li, Q. M. Zhang and M. Gu, *Science*, 2016, **352**, 805–809.
8 R. F. Oulton, V. J. Sorger, T. Zentgraf, R. M. Ma, C. Gladden, L. Dai, G. Bartal and X. Zhang, *Nature*, 2009, **461**, 629–632.
9 K. Saha, S. S. Agasti, C. Kim, X. Li and V. M. Rotello, *Chem. Rev.*, 2012, **112**, 2739–2779.
10 B. Kang, M. M. Afifi, L. A. Austin and M. A. El-Sayed, *ACS Nano*, 2013, **7**, 7420–7427.
11 E. C. Dreaden, A. M. Alkilany, X. Huang, C. J. Murphy and M. A. Elsayed, *Chem. Soc. Rev.*, 2012, **41**, 2740–2779.
12 G. Leveque and O. J. F. Martin, *Opt. Express*, 2006, **14**, 9971–9981.
13 O. L. Muskens, V. Giannini, J. A. Sanchez-Gil and J. G. Rivas, *Opt. Express*, 2007, **15**, 17736–17746.
14 J. J. Mock, R. T. Hill, A. Degiron, S. Zauscher, A. Chilkoti and D. R. Smith, *Nano Lett.*, 2008, **8**, 2245–2252.
15 D. Y. Lei, A. I. Fernandez-Dominguez, Y. Sonnefraud, K. Appavoo, J. Haglund, F. Richard, J. B. Pendry and S. A. Maier, *ACS Nano*, 2012, **6**, 1380–1386.
16 G.-C. Li, Y.-L. Zhang and D. Y. Lei, *Nanoscale*, 2016, **8**, 7119–7126.
17 M. A. Schmidt, D. Y. Lei, L. Wondraczek, V. Nazabal and S. A. Maier, *Nat. Commun.*, 2012, **3**, 1108.
18 D. Y. Lei, A. Aubry, S. A. Maier and J. B. Pendry, *New J. Phys.*, 2010, **12**, 093030.
19 Q. Zhang, G. C. Li, T. W. Lo and D. Y. Lei, *J. Opt.*, 2018, **20**, 024010.
20 A. Aubry, D. Y. Lei, S. A. Maier and J. B. Pendry, *ACS Nano*, 2011, **5**, 3293–3308.
21 J.-X. Li, Y. Xu, Q.-F. Dai, S. Lan and S.-L. Tie, *Laser Photonics Rev.*, 2016, **10**, 826–834.
22 M. Mesch, B. Metzger, M. Hentschel and H. Giessen, *Nano Lett.*, 2016, **16**, 3155–3159.
23 G.-C. Li, Y.-L. Zhang, J. Jiang, Y. Luo and D. Y. Lei, *ACS Nano*, 2017, **11**, 3067–3080.
24 J. Mertens, M.-E. Kleemann, R. Chikkaraddy, P. Narang and J. J. Baumberg, *Nano Lett.*, 2017, **17**, 2568–2574.
25 E. Dulkeith, T. Niedereichholz, T. A. Klar, J. Feldmann, G. von Plessen, D. I. Gittins, K. S. Mayya and F. Caruso, *Phys. Rev. B: Condens. Matter Mater. Phys.*, 2004, **70**, 205424.
26 K.-Q. Lin, J. Yi, S. Hu, J.-J. Sun, J.-T. Zheng, X. Wang and B. Ren, *ACS Photonics*, 2016, **3**, 1248–1255.
27 M. Yorulmaz, S. Khatua, P. Zijlstra, A. Gaiduk and M. Orrit, *Nano Lett.*, 2012, **12**, 4385–4391.
28 Q. Zhao, J. Zhou, F. Zhang and D. Lippens, *Mater. Today*, 2009, **12**, 60–69.
29 J. Li, N. Verellen, D. Vercruysse, T. Bearda, L. Lagae and P. Van Dorpe, *Nano Lett.*, 2016, **16**, 4396–4403.
30 M. W. Knight, Y. Wu, J. B. Lassiter, P. Nordlander and N. J. Halas, *Nano Lett.*, 2009, **9**, 2188–2192.
31 A. Rose, T. B. Hoang, F. McGuire, J. J. Mock, C. Ciracì, D. R. Smith and M. H. Mikkelsen, *Nano Lett.*, 2014, **14**, 4797–4802.
32 H. Chen, T. Ming, S. Zhang, Z. Jin, B. Yang and J. Wang, *ACS Nano*, 2011, **5**, 4865–4877.

33  N. G. Bastus, J. Comenge and V. Puntes, *Langmuir*, 2011, **27**, 11098–11105.

34  R. Alaee, R. Filter, D. Lehr, F. Lederer and C. Rockstuhl, *Opt. Lett.*, 2015, **40**, 2645–2648.

35  Z. Qian, Z. Ji, Z. Fuli and D. Lippens, *Mater. Today*, 2009, **12**, 60–69.

36  Q. Dai, M. Ouyang, W. Yuan, J. Li, B. Guo, S. Lan, S. Liu, Q. Zhang, G. Lu and S. Tie, *Adv. Mater.*, 2017, **29**, 1701918.

37  X. Li, Y. Cao, N. Tian, L. Fu and M. Gu, *Optica*, 2015, **2**, 567–570.

38  J. J. Mock, R. T. Hill, Y.-J. Tsai, A. Chilkoti and D. R. Smith, *Nano Lett.*, 2012, **12**, 1757–1764.

39  C. Lumdee, B. Yun and P. G. Kik, *ACS Photonics*, 2014, **1**, 1224–1230.

40  F. Zhou, Y. Liu and W. Cai, *Opt. Lett.*, 2014, **39**, 1302–1305.

41  A. Li, S. Isaacs, I. Abdulhalim and S. Z. Li, *J. Phys. Chem. C*, 2015, **119**, 19382–19389.

42  A. Sobhani, A. Manjavacas, Y. Cao, M. J. McClain, F. Javier Garcia de Abajo, P. Nordlander and N. J. Halas, *Nano Lett.*, 2015, **15**, 6946–6951.

43  E. Xifre-Perez, L. Shi, U. Tuzer, R. Fenollosa, F. Ramiro-Manzano, R. Quidant and F. Meseguer, *ACS Nano*, 2013, **7**, 664–668.

44  R. Chikkaraddy, X. Zheng, F. Benz, L. J. Brooks, B. de Nijs, C. Carnegie, M.-E. Kleemann, J. Mertens, R. W. Bowman, G. A. E. Vandenbosch, V. V. Moshchalkov and J. J. Baumberg, *ACS Photonics*, 2017, **4**, 469–475.

45  D.-K. Lim, K.-S. Jeon, J.-H. Hwang, H. Kim, S. Kwon, Y. D. Suh and J.-M. Nam, *Nat. Nanotechnol.*, 2011, **6**, 452–460.

46  C. Lumdee, B. Yun and P. G. Kik, *J. Phys. Chem. C*, 2013, **117**, 19127–19133.

47  J. Xiang, S. Jiang, J.-D. Chen, J.-X. Li, Q.-F. Dai, C.-Y. Zhang, Y. Xu, S.-L. Tie and S. Lan, *Nano Lett.*, 2017, **17**, 4853–4859.

48  T. Haug, P. Klemm, S. Bange and J. M. Lupton, *Phys. Rev. Lett.*, 2015, **115**, 067403.

49  P. B. Johnson and R. W. Christy, *Phys. Rev. B: Condens. Matter Mater. Phys.*, 1972, **6**, 4370–4379.

50  A. Otto, *Z. Phys. A: Hadrons Nucl.*, 1968, **216**, 398–410.